



HAL
open science

In-Depth Atomic Mapping of Polarization Switching in a Ferroelectric Field-Effect Transistor

Xiaoyan Li, Qiuxiang Zhu, Lorenzo Vistoli, Agnès Barthélémy, M Bibes, Stéphane Fusil, Vincent Garcia, Alexandre Gloter

► **To cite this version:**

Xiaoyan Li, Qiuxiang Zhu, Lorenzo Vistoli, Agnès Barthélémy, M Bibes, et al.. In-Depth Atomic Mapping of Polarization Switching in a Ferroelectric Field-Effect Transistor. *Advanced Materials Interfaces*, 2020, 7 (14), pp.2000601. 10.1002/admi.202000601 . hal-02984525

HAL Id: hal-02984525

<https://hal.science/hal-02984525>

Submitted on 31 Oct 2020

HAL is a multi-disciplinary open access archive for the deposit and dissemination of scientific research documents, whether they are published or not. The documents may come from teaching and research institutions in France or abroad, or from public or private research centers.

L'archive ouverte pluridisciplinaire **HAL**, est destinée au dépôt et à la diffusion de documents scientifiques de niveau recherche, publiés ou non, émanant des établissements d'enseignement et de recherche français ou étrangers, des laboratoires publics ou privés.

Article type: Full paper

In-depth atomic mapping of polarization switching in a ferroelectric field-effect transistor

X. Li^{1‡}, Q. Zhu^{2‡}, L. Vistoli², A. Barthélémy², M. Bibes², S. Fusil^{2,3}, V. Garcia^{2}, A. Gloter^{1*}*

‡These authors contributed equally to this work

**e-mail:* vincent.garcia@cnrs-thales.fr & alexandre.gloter@u-psud.fr

¹Laboratoire de Physique des Solides, CNRS, Université Paris-Saclay, 91405 Orsay, France

²Unité Mixte de Physique, CNRS, Thales, Université Paris-Saclay, 91767 Palaiseau, France

³Université d'Evry, Université Paris-Saclay, Evry, France

Keywords: Mott transistor, ferroelectric field effect, ferroelectric domains, electronic charge modulation, scanning transmission electron microscopy, electron-energy loss spectroscopy

Abstract

The ferroelectric control of a Mott transistor is a promising strategy for non-volatile low-power electronics. Understanding the fundamental limits of the ferroelectric-field effect is challenging, as the relevant length scales are restricted to a few atomic planes within the interface. Here we investigate the polarization switching process of a prototypical ferroelectric Mott transistor combining BiFeO₃, a ferroelectric material with a large polarization, and (Ca,Ce)MnO₃, a charge-transfer insulator in which a few percent of Ce doping triggers a metal-insulator transition. While scanning probe microscopy indicates a complete switching of the ferroelectric gate, in-depth atomic-scale polarization mapping with scanning transmission electron microscopy reveals incomplete polarization reversal at the interface. Therefore, transport measurements show that the electronic properties of the Mott channel are virtually unchanged by the polarization direction. Nevertheless, in nanometer size areas where interfacial polarization switching occurs, dramatic changes of the electronic properties of (Ca,Ce)MnO₃ are revealed. These results indicate how the performance of mesoscale Mott devices is hindered, and at the same time reveal the possibility of nanoscale energy-efficient Mott transistors.

1. Introduction

Ferroelectrics possess a spontaneous polarization that is switchable by an electric field. These materials can induce non-volatile electron or hole doping in an underlying semiconductor channel, depending on the polarization direction. The amplitude of the ferroelectric-field effect depends both on the polarization magnitude at the interface and on the charge-modulated sensitivity of the channel material. In Mott insulators, the insulating character arises from strong electronic correlations, opening a gap between occupied and empty d levels. Their insulating state can be destabilized by external stimuli, such as electric fields, inducing a transition to a metallic state. Hence, employing to Mott insulator channels is expected to increase the resistance change associated to polarization reversal, as compared to standard semiconductor channels.

As a channel material, we use a Ce-doped calcium manganite. In bulk, CaMnO_3 is a G-type antiferromagnetic insulator^[1]. It crystallizes in the paraelectric $Pnma$ orthorhombic ground-state structure where the tilting of oxygen octahedra produces a small distortion from the cubic structure of the perovskite. The chemical substitution of Ca^{2+} by Ce^{4+} in orthorhombic $\text{Ca}_{1-x}\text{Ce}_x\text{MnO}_3$ manganites gives two electrons in the Mn-3d (e_g) band which induces a transition to a metallic state at around $x = 5\%$ ^[1]. Thus, the metal-insulator transition occurs at much lower carrier concentrations in the electron-doped $(\text{Ca,Ce})\text{MnO}_3$ than in widely investigated hole-doped manganites such as $(\text{La,A})\text{MnO}_3$ ($A=\text{Ca, Sr}$) ^[2]. This makes electron-doped manganites very appealing in view of integrating them as channel materials in oxide-based field effect transistors where metal-insulator transitions can be triggered by an electric field. In thin films of $(\text{Ca,Ce})\text{MnO}_3$, the epitaxial strain imposed by the substrate has a profound effect on the phase diagram of the electron-doped manganite ^[3]. Indeed, compressive strain (-0.5% for CaMnO_3 on YAlO_3 substrates) results in the stabilization of the metallic state at much lower doping ($x > 2\%$) than in the bulk ^[4].

As a ferroelectric gate, we focus on bismuth ferrite. BiFeO₃ is a room temperature multiferroic and the ferroelectric with the largest polarization (100 $\mu\text{C}/\text{cm}^2$ in the bulk)^[5]. While bulk BiFeO₃ crystallizes in a pseudocubic R3c structure, a strongly elongated polymorph can be stabilized in thin films at large compressive strain (> 4%). This so-called tetragonal-like phase has an even larger polarization^[6-8]. Furthermore, its relatively small in-plane lattice constant compared with conventional oxide ferroelectrics (BaTiO₃, Pb(Zr,Ti)O₃, etc.) makes it compatible with a broad range of strongly distorted orthorhombic perovskites such as (Ca,Ce)MnO₃ and YAlO₃.

2. Results and discussion

The X-ray diffraction 2 Θ - ω scan (Supplementary Information) of the samples shows that BiFeO₃ is purely in the highly-strained super-tetragonal phase. Additionally, Laue fringes of both the BiFeO₃ and Ca_{0.96}Ce_{0.04}MnO₃ peaks are visible, attesting the coherent growth of both films.

BiFeO₃/Ca_{0.96}Ce_{0.04}MnO₃ bilayers were patterned by optical lithography and argon ion etching into Hall bars (**Figure 1a**). Piezoresponse force microscopy (PFM) indicates that the ferroelectric polarization of BiFeO₃ is initially pointing downwards (towards the manganite channel), in accordance with the imprint of the piezoelectric loop to positive bias (**Figure 1b**). In order to switch the polarization of BiFeO₃ from downwards to upwards, we applied a positive dc voltage to the Ca_{0.96}Ce_{0.04}MnO₃ electrode while scanning the Hall bar with the PFM tip. The Hall bar polarization is reversed as evidenced by a clear phase contrast of 180 degrees in the out-of-plane PFM image (**Figure 1a**). We probed the influence of polarization direction on the resistance and the carrier concentration of Ca_{0.96}Ce_{0.04}MnO₃ through electronic transport measurements. In BiFeO₃/Ca_{0.96}Ce_{0.04}MnO₃, the reversal of the ferroelectric polarization

induces only tiny variations in both longitudinal (**Figure 1c**) and transverse (**Figure 1d**) resistance measurements. The lack of a significant ferroelectric field effect was also observed for other compositions of $(\text{Ca,Ce})\text{MnO}_3$ with Ce doping ranging from 1 to 5% (Supplementary Information). This negligible variation of carrier density is in stark contrast with expectations from both the polarization of BiFeO_3 and the phase diagram of $(\text{Ca,Ce})\text{MnO}_3$. Indeed, a polarization of $100 \mu\text{C}/\text{cm}^2$ for BiFeO_3 would lead to an equivalent charge modulation of $1.25 \times 10^{15} \text{ cm}^{-2}$ in the manganite channel. $\text{Ca}_{0.96}\text{Ce}_{0.04}\text{MnO}_3$ contains 0.08 electrons per unit cell corresponding to carrier densities of typically around $1.55 \times 10^{21} \text{ cm}^{-3}$, as confirmed by Hall measurements ($1.1\text{-}1.6 \times 10^{21} \text{ cm}^{-3}$). For a film thickness of 20 nm, the sheet carrier density is then $3.1 \times 10^{15} \text{ cm}^{-2}$. Polarization reversal would thus be equivalent to a change in chemical doping from about 3% to 5%, leading in principle to significant changes in the conduction [9]. The lack of transport signatures for sharp phase transition in $\text{Ca}_{0.96}\text{Ce}_{0.04}\text{MnO}_3$ upon ferroelectric switching could be related to different mechanisms. First, the large thickness of the channel compared to the Thomas-Fermi screening length of few nanometers could lead to a parallel conduction between a charge-modulated layer and an “unaffected” metallic channel that would act as short circuit. Second, the full efficiency of the ferroelectric field effect is impeded by interfacial pinning [10,11].

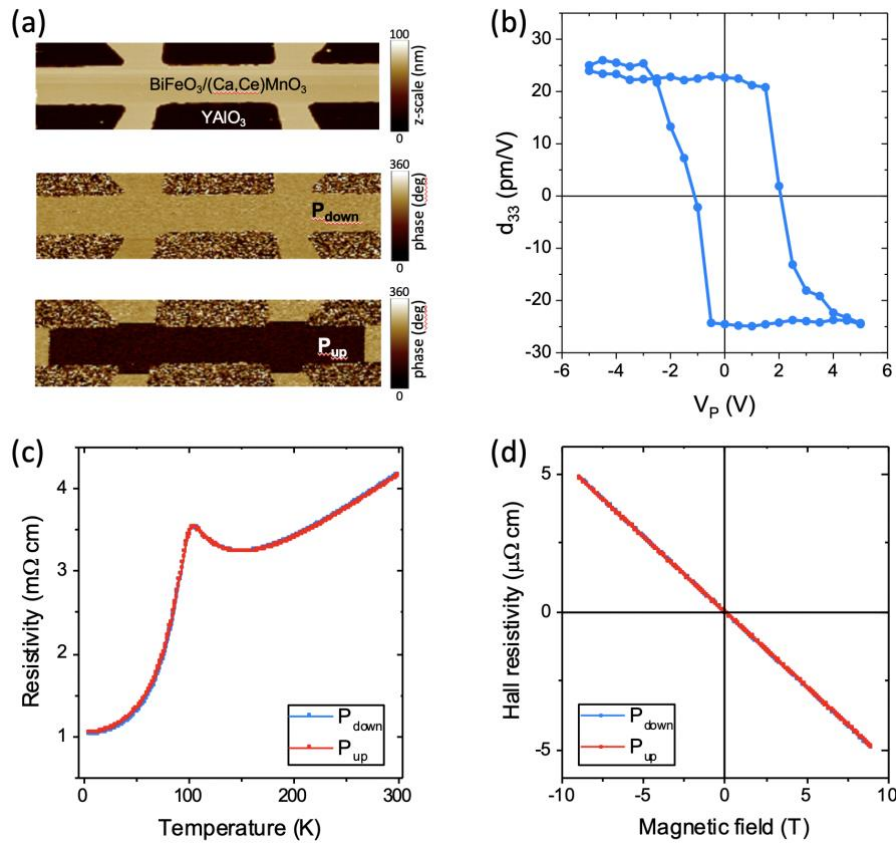


Figure 1. BiFeO₃/(Ca,Ce)MnO₃ ferroelectric field-effect devices. a) Combined topography and PFM phase image of the Hall bar before and after switching the polarization from downwards to upwards. The width of the Hall bar is 10 μm. b) Local piezoelectric loop of the ferroelectric device with a voltage applied to the manganite electrode. c) Temperature dependence of the resistivity and d) room-temperature Hall resistivity of the BiFeO₃/Ca_{0.96}Ce_{0.04}MnO₃ for the virgin (blue) and switched (red) states.

In order to get more insights into these pending questions, we conducted Cs-corrected scanning transmission electron microscopy (STEM) and electron-energy loss spectroscopy (EELS) experiments to correlate structural and charge distribution for both polarization states. The sample was ex-situ polarized by the PFM tip in $1 \times 10 \mu\text{m}^2$ areas separated by 1 μm gap of unswitched areas to observe different polarized states and the corresponding field effect under the same experimental conditions. In these different areas, the writing voltage was varied from

about one to three times the coercive field. Flat and thin lamellas were prepared using focus ion beam (FIB) to allow the observations of the different regions. The samples were prepared at both $[110]_{pc}$ and $[100]_{pc}$ zone axis of the YAlO_3 substrate. The microstructure of the epitaxial stack was investigated in Cs corrected STEM, utilizing atomically resolved high angle annular dark field imaging (HAADF), and annular bright field imaging (ABF), with a typical spatial resolution of 70 pm. The corresponding interfacial chemical distribution and charge quantification were studied by EELS spectrum imaging.

The STEM-HAADF of the heterostructure (**Figure 2a**) indicates that the films are epitaxial with well-defined interfaces and that the BiFeO_3 is in its super-tetragonal phase ($c/a = 1.25 \pm 0.03$). The atomic structure of BiFeO_3 can be seen in more details in **Figure 2b** for the initial downwards polarization and in **Figure 2c** for the (switched) upwards polarization. In order to achieve a better oxygen contrast in STEM-ABF images, the film is oriented at the $[110]_{pc}$ zone axis^[12]. Both HAADF and ABF images are shown as well as their RGB combination. The RGB image indicates large O and Fe displacements for both polarization orientations. In the ABF image, the off-center displacements are found to be around 0.82 Å for the O anion and 0.38 Å for the Fe cation along the same direction, corresponding to polarization values in the order of $100 \mu\text{C}/\text{cm}^2$ ^[13]. This implies that the electric field applied by PFM has enabled to switch the polarization and that the ferroelectric retention is maintained during the STEM specimen preparation. As observed for other perovskites^[13,14], the ferroelectric polarization direction appears opposite to the off-centering of the Fe cation. This means that the ferroelectric polarization can be mapped using only the STEM-HAADF image contrast, that is quicker than a systematic ABF/HAADF dual acquisition.

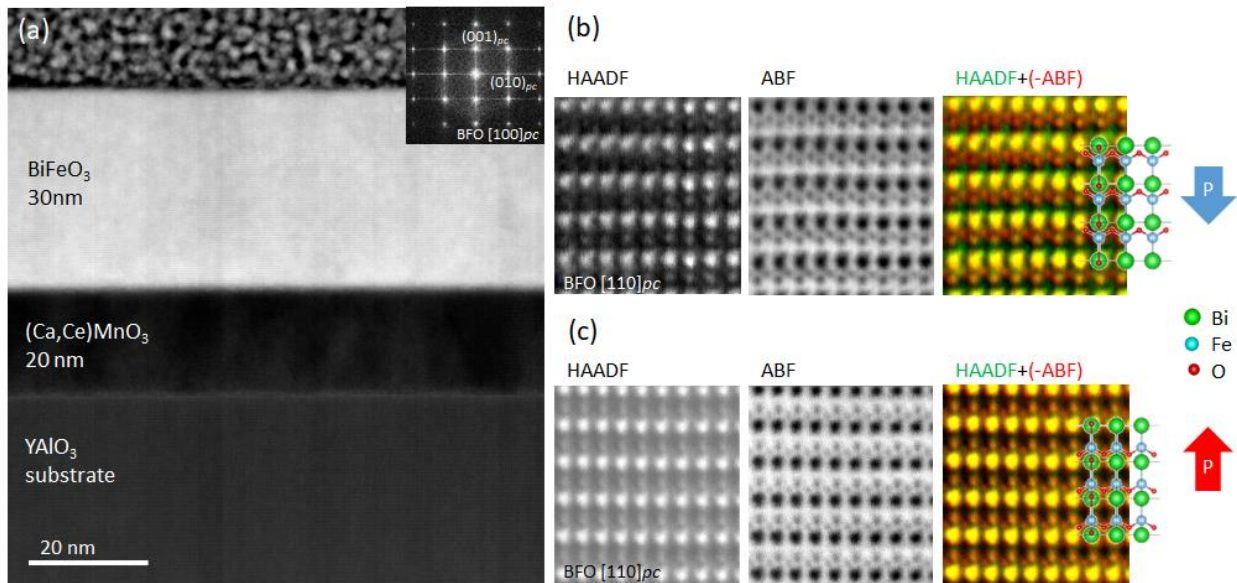


Figure 2. a) STEM-HAADF image of $\text{BiFeO}_3/(\text{Ca,Ce})\text{MnO}_3$ heterostructure grown on YAlO_3 substrate, at the $[100]_{pc}$ zone axis. Insert is the fast Fourier transform (FFT) of BFO thin film indicating a super-tetragonal structure. $[110]_{pc}$ zone axis STEM-HAADF, ABF and the RGB mixture of the corresponding HAADF and ABF image for (b) downwards and (c) upwards polarization states, respectively. The atomic models of different polarizations are overlapped with the corresponding RGB images.

The statistical analysis of the domain distribution was realized by atomically resolved STEM-HAADF images in regions polarized upwards by PFM. **Figure 3** shows eight $64 \times 64 \text{ nm}^2$ images obtained from a single representative region polarized upwards. The upwards domains are highlighted in red in the HAADF images. Surprisingly, the switching of polarization is incomplete with 31% to 91% of the volume population with upwards polarization (62% in average). The upwards domains seem to nucleate from the top surface of the BiFeO_3 layer and propagate toward the $\text{BiFeO}_3/\text{Ca}_{0.96}\text{Ce}_{0.04}\text{MnO}_3$ interface. However, only 19% of the interface is successfully switched. This statistical analysis was performed on another switched region giving similar conclusions with an average switched volume of 65% and only 5% of switched regions at the interface (**Figure S1**). The inhomogeneous domain distribution observed by

STEM-HAADF is apparently inconsistent with the homogeneous PFM phase signal from switched regions (**Figure 1a**). In reality, the out-of-plane PFM phase signal detected under the tip is intrinsically binary and determined by the dominant polarization along the vertical axis of the film, for each measurement location. An inhomogeneous distribution of polarization along this axis would only lead to a decrease in the PFM amplitude signal. Therefore, the typical STEM observations from **Figure 3** would result in an apparently homogeneous PFM phase signal, as long as the fraction of switched domains is larger than 50% in the volume. This explains the very low ratio of ferroelectric field effect measured on similar heterostructures by transport measurements (**Figure 1c-d**).

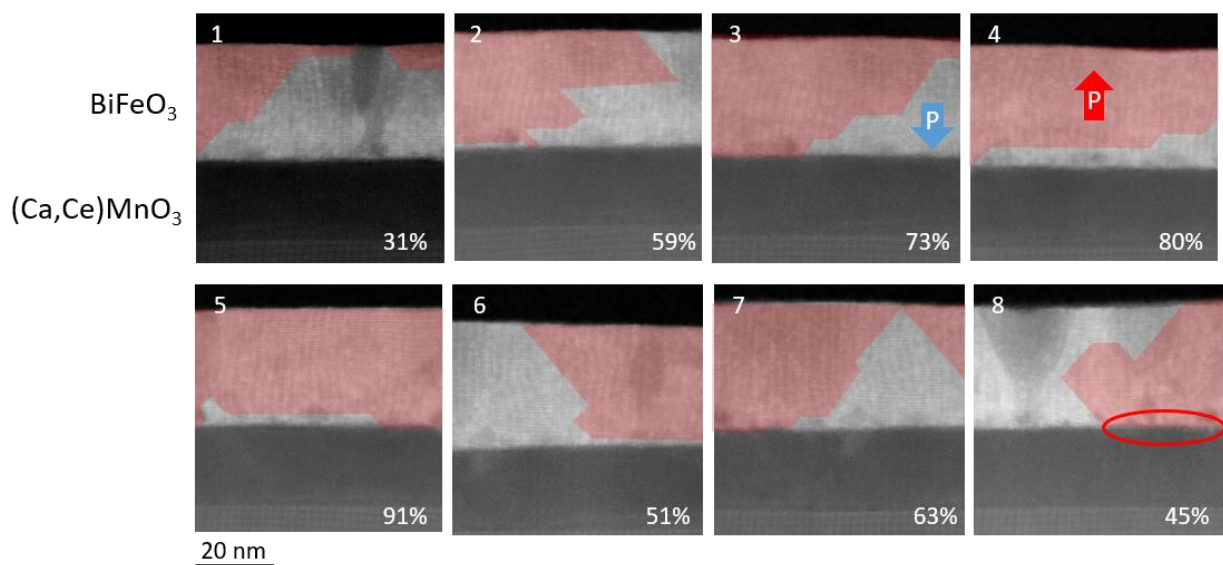


Figure 3. STEM-HAADF overview of the BiFeO₃ upwards polarization region defined by PFM, the upwards domains are marked with red overprint and their volume percentage in each image is written at the bottom right. The upwards polarization can also be observed at the interface with the (Ca,Ce)MnO₃ as, for example, marked by the red ellipse.

The difference between the switched volume and the switched interface suggests the existence of an interfacial barrier that limits the propagation of the upwards domains down to the $\text{Ca}_{0.96}\text{Ce}_{0.04}\text{MnO}_3$ interface. Similarly, unswitched domains close to the interface were reported for $\text{PbZr}_{0.2}\text{Ti}_{0.8}\text{O}_3$ thin films grown on Nb-doped SrTiO_3 [13]. Their stability is interpreted by the electric field associated to the band bending at the interface. Furthermore, previous works have shown that specific polar plane terminations favor one polarization state over the other due to additional interfacial dipoles [11]. For instance, $\text{BiO-FeO}_2\text{-CaO-MnO}_2$ sequences observed for the interface between BiFeO_3 and CaMnO_3 are expected to favor the downwards polarization state [16]. In addition, EELS analysis for the O-K and Fe-L evidence the presence of holes at the BiFeO_3 surface for the unswitched regions (downwards polarization) (**Figure S2**). Therefore, both the interface dipoles and surface charges seem to favor the downwards polarization of BiFeO_3 . Nevertheless, the surface density of holes is strongly reduced in switched regions (upwards polarization) of BiFeO_3 (**Figure S2**), in accordance with the stability of upwards polarized domains close to the surface (**Figure 3**).

While the small fraction of switched polarization at the interface impedes the observation of any field effect from BiFeO_3 at the micron scale, some areas did successfully switch at the nanometer scale. We now focus on the interfacial electronic properties of the $\text{Ca}_{0.96}\text{Ce}_{0.04}\text{MnO}_3$ layer in these regions, where we investigate the electrostatic carrier modulation by the EELS near-edge fine structure. Two typical defect-free interfaces with an atomically sharp termination and opposite polarization were selected. The EELS spectrum images were collected throughout the whole $\text{Ca}_{0.96}\text{Ce}_{0.04}\text{MnO}_3$ layer and its interfaces with both BiFeO_3 and YAlO_3 . The RGB image constructed from the Fe (blue), Ca (green) and Mn (red) EELS signals is shown in **Figure 4a** and **c**, for the downwards and upwards polarization states, respectively. The corresponding zoomed in STEM-HAADF images at the $\text{BiFeO}_3/\text{Ca}_{0.96}\text{Ce}_{0.04}\text{MnO}_3$ interface can be found in **Figure 4b** and **d**, respectively. The off-center displacements of the Fe atoms indicate that the

opposite ferroelectric polarizations are preserved down to the interface with $\text{Ca}_{0.96}\text{Ce}_{0.04}\text{MnO}_3$. The interface sequence is $(\text{FeO}_2)^-(\text{Ca}_{0.96}\text{Ce}_{0.04}\text{O})^{0.08+}$ in both cases, indicating a fix interfacial dipole pointing toward $\text{Ca}_{0.96}\text{Ce}_{0.04}\text{MnO}_3$ [11].

The chemical shift of the Mn- L_3 edge across the $\text{Ca}_{0.96}\text{Ce}_{0.04}\text{MnO}_3$ layer is displayed in **Figure 4e** for both polarization states. It reflects changes of the oxidation state of Mn upon electron doping. The nominal Mn valence of +3.92 in stoichiometric $\text{Ca}_{0.96}\text{Ce}_{0.04}\text{MnO}_3$ is set as reference zero in the profile. The corresponding profiles of the excess electron density (**Figure 4f**) are deduced from the chemical shift of Mn- L_3 edge (**Figure S3**), considering its correspondence with the Mn valence¹⁵. In the middle of the $\text{Ca}_{0.96}\text{Ce}_{0.04}\text{MnO}_3$ layer, the charge profiles present a plateau zone for around 10 nm while deviations from the nominal oxidation state are observed near the two interfaces. Near the YAlO_3 interface, we observe a large electron accumulation region of 20 unit-cells, which does not depend on polarization. This region is attributed to an “insulating dead layer” measured in the transport properties of ultrathin films [17]. Close to the BiFeO_3 interface, the excess electron density of the first 5 nm of $\text{Ca}_{0.96}\text{Ce}_{0.04}\text{MnO}_3$ is strongly dependent on the polarization direction. Once integrated within the first 13 unit-cells from the interface, the downwards polarization leads to an electron accumulation of $2.3 e^-$ in $\text{Ca}_{0.96}\text{Ce}_{0.04}\text{MnO}_3$, while the upwards polarization generates an effective electron depletion of $0.1 e^-$. The charge modulation is asymmetric with respect to the nominal Mn valence. Several reasons, such as the complex hole and electron doping energetic landscape in $(\text{Ca,Ce})\text{MnO}_3$ [Husanu et al. 2020], an electron doping offset close to the interface, or the difference in the BiFeO_3 depolarizing field for both states [Jiang et al. 2013], might explain such asymmetry. Consequently, ferroelectric switching induces an effective charge modulation of $2.4 e^-$ in the manganite corresponding to a sheet carrier density variation of $17 \times 10^{14} \text{ cm}^{-2}$. This is within the range of the modulation expected for super-tetragonal BiFeO_3 with a polarization of the order of $130 \mu\text{C}\cdot\text{cm}^{-2}$ (i.e., $16 \times 10^{14} \text{ cm}^{-2}$). These experiments demonstrate that, while only

a minor fraction of ferroelectric domains switch at the interface, the ferroelectric field-effect is very efficient at the local scale.

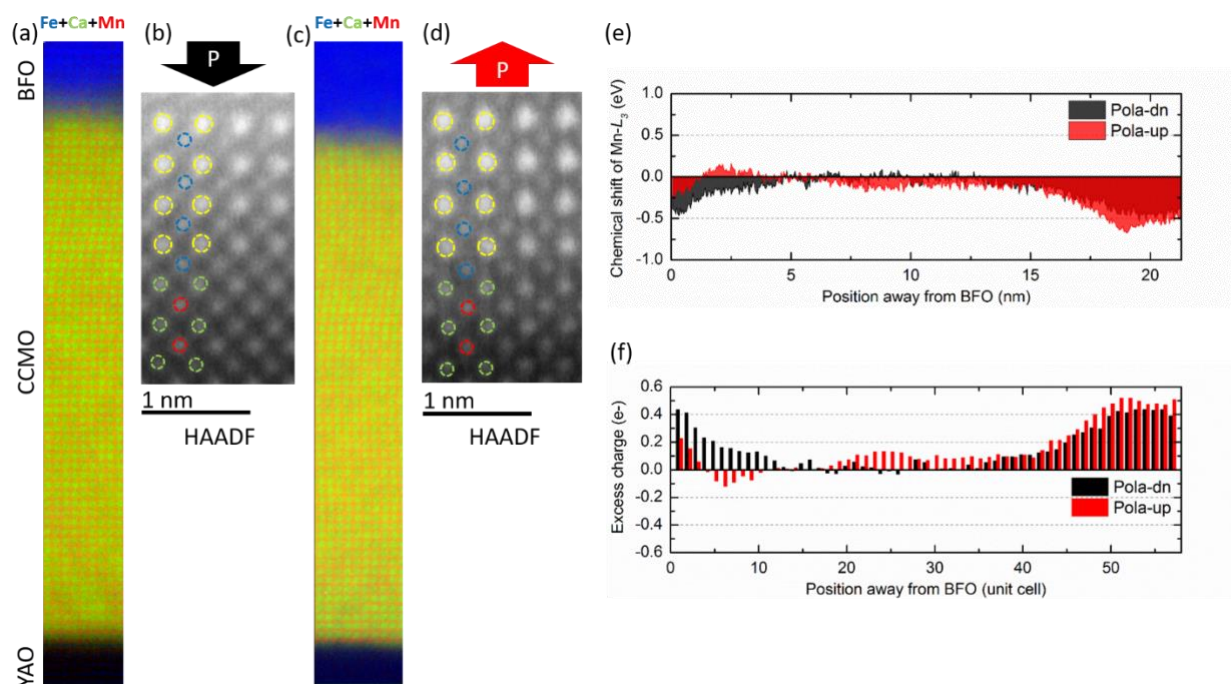


Figure 4. The RGB images constructed by the atomic EELS chemical mapping of Fe- $L_{2,3}$ (blue), Ca- $L_{2,3}$ (green) and Mn- $L_{2,3}$ (red) across the $\text{Ca}_{0.96}\text{Ce}_{0.04}\text{MnO}_3$ thin film for (a) downwards and (c) upwards polarization states, respectively. HAADF images of the corresponding $\text{BiFeO}_3/\text{Ca}_{0.96}\text{Ce}_{0.04}\text{MnO}_3$ interfaces for (b) downwards and (d) upwards polarization states, where the Bi, Fe, Ca, and Mn atoms are indicated by yellow, blue, green and red open circles, respectively. (e) Chemical shift of Mn- L_3 edge and (f) the excess charge per unit cell scale across the $(\text{Ca,Ce})\text{MnO}_3$ layer for the downwards (black) and upwards (red) polarization states. The zero reference of the profile is the nominal stoichiometry $\text{Ca}_{0.96}\text{Ce}_{0.04}\text{MnO}_3$ where the Mn valence is +3.92 with Mn- L_3 edge at 641.31 eV.

3. Conclusion

The ferroelectric field-effect device under focus here is based on a combination of a ferroelectric BiFeO₃ and a doped Mott insulator Ca_{0.96}Ce_{0.04}MnO₃. It was investigated thanks to the ex-situ switching of polarization at the micron scale by piezoresponse force microscopy and subsequent STEM-EELS observations on cross-section specimens. This approach is ideally suited to provide key information on polarization switching phenomena at interfaces and their influence on the electronic properties of the adjacent layer. The real space and spectroscopic observations at the atomic scale indicate that the “switched” regions actually consist of heterogeneous configurations with various fractions of upwards/downwards polarization domains in the volume of the ferroelectric. The striking feature is that the fraction of switched domains is below 20% at the interface. This precludes any efficient field-effect as measured by “macroscopic” transport experiments. Nevertheless, we demonstrate that nanoregions with switched interfacial polarization generate large variations of the carrier concentrations in the adjacent manganite layer, consistently with the large polarization of BiFeO₃. The manganite channel thickness affected by polarization switching is found to be about 5 nm. These results hold promises for the practical developments of ferroelectric field-effect transistors and other non-volatile low power devices.

4. Experimental Section

The BiFeO₃/Ca_{0.96}Ce_{0.04}MnO₃ bilayers on YAlO₃ (001) substrates were grown by pulsed laser deposition using a frequency-tripled Nd:YAG laser with a wavelength of 355 nm. The YAlO₃

substrates were first annealed in a furnace under oxygen flow at 1000°C for 2.5 hours. 20-nm-thick $\text{Ca}_{0.96}\text{Ce}_{0.04}\text{MnO}_3$ epilayers were grown at 620°C under an oxygen pressure of 0.2 mbar and a fluence of 1.45 J/cm². Successively, we deposited the 30-nm-thick BiFeO_3 layer with a substrate temperature of 430°C, an oxygen pressure of 0.006 mbar and a fluence of 0.42 J/cm². Post-growth annealing was then performed at 350°C by increasing the oxygen pressure to 300 mbar for 30 minutes.

Flat and thin lamellas were prepared using focus ion beam (FIB) and Easylift technique (Scios DualBeam, FEI). The STEM experiments were done using a NION UltraSTEM200 C3/C5-corrected STEM, at a voltage of 100 keV, in order to limit the beam damage. EELS spectra were collected using a in-house detector based on a ProEM EMCCD Cameras from Princeton Instruments.

Supporting Information

Figure S1. PFM phase image of BiFeO₃/Ca_{0.96}Ce_{0.04}MnO₃ thin film and the corresponding STEM-HAADF overview of the BiFeO₃ upwards polarized regions.

Figure S2. BiFeO₃ surface charge investigation by EELS.

Figure S3. Ca_{0.96}Ce_{0.04}MnO₃ interface charge investigation by EELS. Extracted Mn-L and O-K spectra.

Acknowledgements

We thank support from the Collaborative Research center SFB762 ‘Functionality of Oxide Interfaces’. This research received financial support from the ERC Consolidator grant ‘MINT’ (contract no. 615759) and ANR projects ‘FERROMON’, ‘PIAF’ and ‘EXPAND’. This work was also supported by a public grant overseen by the ANR as part of the ‘Investissement d’Avenir’ programme (LABEX NanoSaclay, ref. ANR-10-LABX-0035) through projects ‘FERROMOTT’ and ‘AXION’.

Received: ((will be filled in by the editorial staff))

Revised: ((will be filled in by the editorial staff))

Published online: ((will be filled in by the editorial staff))

References

- [1] CE. N. Caspi, M. Avdeev, S. Short, J. D. Jorgensen, M. V. Lobanov, Z. Zeng, M. Greenblatt, P. Thiyagarajan, C. E. Botez, P. W. Stephens, *Physical Review B* **2004**, *69*.
- [2] C. H. Ahn, J.-M. Triscone, J. Mannhart, *Nature* **2003**, *424*, 1015.
- [3] P.-H. Xiang, H. Yamada, H. Akoh, A. Sawa, *Journal of Applied Physics* **2012**, *112*, 113703.
- [4] P.-H. Xiang, S. Asanuma, H. Yamada, I. H. Inoue, H. Sato, H. Akoh, A. Sawa, K. Ueno, H. Yuan, H. Shimotani, M. Kawasaki, Y. Iwasa, *Advanced Materials* **2011**, *23*, 5822.5.
- [5] D. Lebeugle, D. Colson, A. Forget, M. Viret, P. Bonville, J. F. Marucco, S. Fusil, *Physical Review B* **2007**, *76*.
- [6] D. Ricinschi, K.-Y. Yun, M. Okuyama, *Journal of Physics: Condensed Matter* **2006**, *18*, L97.
- [7] H. Béa, B. Dupé, S. Fusil, R. Mattana, E. Jacquet, B. Warot-Fonrose, F. Wilhelm, A. Rogalev, S. Petit, V. Cros, A. Anane, F. Petroff, K. Bouzehouane, G. Geneste, B. Dkhil, S. Lisenkov, I. Ponomareva, L. Bellaiche, M. Bibes, A. Barthélémy, *Physical Review Letters* **2009**, *102*.
- [8] X. Zhang, Q. He, M. Trassin, W. Luo, D. Yi, M. D. Rossell, P. Yu, L. You, C. H. Wang, C. Y. Kuo, J. T. Heron, Z. Hu, R. J. Zeches, H. J. Lin, A. Tanaka, C. T. Chen, L. H. Tjeng, Y.-H. Chu, R. Ramesh, *Physical Review Letters* **2011**, *107*.
- [9] VL. Vistoli, W. Wang, A. Sander, Q. Zhu, B. Casals, R. Cichelero, A. Barthélémy, S. Fusil, G. Herranz, S. Valencia, R. Abrudan, E. Weschke, K. Nakazawa, H. Kohno, J. Santamaria, W. Wu, V. Garcia, M. Bibes, *Nature Physics* **2019**, *15*, 67.
- [10] C. T. Nelson, P. Gao, J. R. Jokisaari, C. Heikes, C. Adamo, A. Melville, S.-H. Baek, C. M. Folkman, B. Winchester, Y. Gu, Y. Liu, K. Zhang, E. Wang, J. Li, L.-Q. Chen, C.-B. Eom, D. G. Schlom, X. Pan, *Science* **2011**, *334*, 968.

- [11] YP. Yu, W. Luo, D. Yi, J. X. Zhang, M. D. Rossell, Q. M. Ramasse, R. Erni, L. W. Martin, Y. H. Chu, S. T. Pantelides, S. J. Pennycook, R. Ramesh, *PNAS* **2012**, 109, 9710.
- [12] X. Li, I. Lindfors-Vrejoiu, M. Ziese, A. Gloter, P. A. van Aken, *Scientific Reports* **2017**, 7, 40068.
- [13] C. T. Nelson, B. Winchester, Y. Zhang, S.-J. Kim, A. Melville, C. Adamo, C. M. Folkman, S.-H. Baek, C.-B. Eom, D. G. Schlom, L.-Q. Chen, X. Pan, *Nano Letters* **2011**, 11, 828.
- [14] G.-Y. Kim, K. Chu, K.-D. Sung, H.-S. Lee, S.-D. Kim, K. Song, T. Choi, J. Lee, J. P. Buban, S.-Y. Yoon, K.-H. Kim, C.-H. Yang, S.-Y. Choi, *APL Materials* **2017**, 5, 066104.
- [15] M.-G. Han, M. S. J. Marshall, L. Wu, M. A. Schofield, T. Aoki, R. Twesten, J. Hoffman, F. J. Walker, C. H. Ahn, Y. Zhu, *Nature Communications* **2014**, 5.
- [16] M. Marinova, J. E. Rault, A. Gloter, S. Nemsak, G. K. Palsson, J.-P. Rueff, C. S. Fadley, C. Carrétéro, H. Yamada, K. March, V. Garcia, S. Fusil, A. Barthélémy, O. Stéphan, C. Colliex, M. Bibes, *Nano Letters* **2015**, 15, 2533.
- [17] H. Yamada, M. Marinova, P. Altuntas, A. Crassous, L. Bégon-Lours, S. Fusil, E. Jacquet, V. Garcia, K. Bouzehouane, A. Gloter, J. E. Villegas, A. Barthélémy, M. Bibes, *Scientific Reports* **2013**, 3.

Copyright WILEY-VCH Verlag GmbH & Co. KGaA, 69469 Weinheim, Germany, 2016.

